Title

Branching Ratios in Vacuum Ultraviolet Photodissociation of CO and N2: Implications for Oxygen and Nitrogen Isotopic Compositions of the Solar Nebula

Permalink

https://escholarship.org/uc/item/62s4b93z

Journal

The Astrophysical Journal, 850(1)

ISSN

0004-637X

Authors

Shi, Xiaoyu
Yin, Qing-Zhu
Gao, Hong
et al.

Publication Date

2017-11-20

DOI

10.3847/1538-4357/aa8ee7

Peer reviewed

Branching Ratios in Vacuum Ultraviolet Photodissociation of CO and N₂: Implications for Oxygen and Nitrogen Isotopic Compositions of the Solar Nebula

Xiaoyu Shi[1,2,4] , Qing-Zhu Yin[2] , Hong Gao[1,5], Yih-Chung Chang[1], William M. Jackson[1],
Roger C. Wiens[3], and Cheuk-Yiu Ng[1]

[1] Department of Chemistry, University of California, Davis, CA 95616, USA; cyng@chem.ucdavis.edu
[2] Department of Earth and Planetary Sciences, University of California, Davis, CA 95616, USA; qyin@ucdavis.edu
[3] Los Alamos National Laboratory, Los Alamos, NM 87545, USA

Abstract

NASA's *Genesis* mission reveals that the rare isotope ^{15}N is approximately seven times more enriched than the rare isotopes ^{17}O and ^{18}O in the terrestrial planets relative to the Sun. Here, we explain this peculiar observation under the framework of self-shielding and the difference in chemical reactivity between the excited $O(^1D)$ [$N(^2D)$] and the ground $O(^3P)$ [$N(^4S)$] states produced by VUV photodissociation of CO [N₂]. After weighting the absorption cross-sections for individual photodissociation bands, and taking into account the mutual shielding by H₂, the CO/N₂ ratio, and the partition of O and N among gas:ice:dust phases in the solar nebula, we show that the trapping of $N(^2D)$ via hydrogenation is favored over that of $O(^1D)$. This provides a possible explanation of the *Genesis* results and supports the self-shielding model as the primary mechanism for generating isotopic anomalies of O and N in the early solar nebula.

Key words: astrochemistry – ISM: molecules – meteorites, meteors, meteoroids – protoplanetary disks – solar wind – Sun: abundances

1. Introduction

Oxygen displays significant isotopic heterogeneity among early solar system objects found in primitive meteoritic components and planetary materials with both ^{16}O-rich and ^{16}O-poor reservoirs of equal ^{17}O/^{18}O ratio (Clayton 1993). Since its original discovery, this peculiar distribution of oxygen isotope abundances in the solar system materials (e.g., Clayton 1993; Wiens et al. 1999; McKeegan & Leshin 2001; Yin 2004) has defied explanation for four decades (Clayton et al. 1973).

Recently, building on well-known astronomical observations (Bally & Langer 1982) and earlier suggestions (Thiemens & Heidenreich 1983; Navon & Wasserburg 1985), a theoretical model known as carbon monoxide (CO) self-shielding (COSS) was proposed to explain the observed oxygen isotope anomalies (e.g., Clayton 2002; Yurimoto & Kuramoto 2004; Lyons & Young 2005). Unlike the earlier model that focused on symmetry or self-shielding of minor gas species such as O₃, O₂, and CO₂ (Thiemens & Heidenreich 1983; Navon & Wasserburg 1985), the new COSS model (e.g., Clayton 2002; Yurimoto & Kuramoto 2004; Lyons & Young 2005; Lyons 2014) focused on photochemical isotopic effects of major volatile species such as CO (second in abundance to H₂ in molecular clouds). The model tracks a parcel of dust and gas with an initially homogenous oxygen isotopic composition. When the parcel of materials in a molecular cloud or protoplanetary disk is subjected to vacuum ultraviolet (VUV) radiation from an external source of a nearby star, photo-dissociation of CO occurs. Given a VUV photon intensity distribution, and the different energies of predissociative states and number densities of isotopologues of C^{16}O, C^{17}O, and

C^{18}O, isotope-specific VUV attenuation ("self-shielding") occurs on the edge of molecular clouds or protoplanetary disks facing the incoming VUV light sources. This is a well-known astronomical phenomenon (e.g., Bally & Langer 1982; van Dishoeck & Black 1988) that generates ^{17,18}O-rich atomic oxygen and ^{16}O-rich CO deeper inside the molecular cloud (Sheffer et al. 2002). The highly reactive ^{17,18}O-rich atomic oxygen produced by VUV photodissociation of CO would rapidly react with H₂ molecules to form ^{17,18}O-enriched H₂O, appearing as water-ice mantles on silicate dust grains (Yurimoto & Kuramoto 2004). When the molecular cloud collapses and the young stellar object ignites, its surroundings are heated through radiation and/or shocks that will chemically and thermally process the ice-mantle grains, producing the observed isotopic mixing of ^{16}O-rich and ^{16}O-poor reservoirs with equal ^{17}O/^{18}O ratio (Yin 2004).

The model is significant in that the proposed mechanism and reaction pathways involve all major oxides in the early solar nebula (CO 50%, H₂O ∼33%, and ∼17% oxides of other elements with an overall uncertainty of ±10%; e.g., Wiens et al. 1999; Lodders 2003; Young 2007; Asplund et al. 2009; Yin et al. 2009; Krot et al. 2010). Remnants of the early solar system water and organic species with heavy oxygen and carbon isotopes highly enriched relative to the terrestrial standards have been found recently in primitive meteorites (e.g., Sakamoto et al. 2007; Hashizume et al. 2011). The recent laboratory measurements of the solar wind collected by the *Genesis* mission show that the Sun is depleted in both heavy isotopes of oxygen relative to the Earth and other terrestrial planetary materials (McKeegan et al. 2011) by ∼6%. These observations collectively lend strong support for the COSS model.

Only the VUV wavelength range of 91.17–111.78 nm (13.60–11.09 eV) is of interest to the photochemical COSS model. This is because radiation at shorter wavelengths is largely absorbed by ionization of hydrogen (van Dishoeck &

---

[4] Present address: Department of Pharmaceutical Chemistry, University of California, San Francisco, CA 94158, USA.
[5] Present address: Department of Chemistry, University of Basel, Klingelbergstrasse 80, CH-4056 Basel, Switzerland.

Black 1988; Visser et al. 2009), while the energies of radiation at wavelengths longer than 111.78 nm are lower than the 0 K bond dissociation energy ($D_0 = 11.09$ eV) of CO (Bakker & Parker 2000). Thus, VUV radiation at wavelengths <91.17 nm or >111.78 nm can be ignored in COSS studies.
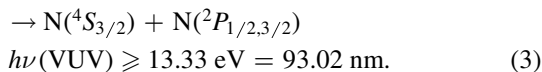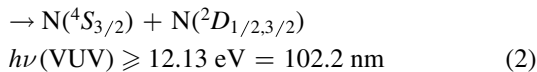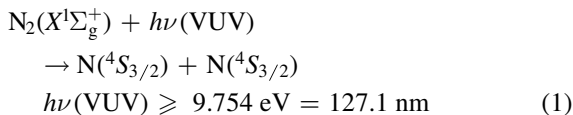
By analogy with CO, it has been suggested (Clayton 2002) that the source of the ^{15}N enrichment in the planetary materials is due to a large nitrogen isotopic fractionation caused by VUV photodissociation of N_2 and isotopic N_2 self-shielding (N2SS) in the molecular cloud prior to or concomitant with its collapse, or in the collapsed protoplanetary disk surface. This is because the isoelectronic molecules CO and N_2 have similar photochemical properties. Photoabsorption, fluorescence, and photoionization studies (e.g., Ajello et al. 1989; Chan et al. 1993) show that CO and N_2 have similar photoabsorption cross-sections and essentially all of the absorption bands of CO and N_2 in the wavelength region of ≈88–110 nm are strongly predissociative in nature (e.g., Zipf & McLaughlin 1978; Letzelter et al. 1987; Ajello et al. 1989; Eidelsberg & Rostas 1990; Chan et al. 1993; Eikema et al. 1994; Vieitez et al. 2008).

The *Genesis* mission team has shown that the Sun, and by inference, the protosolar nebula, is also highly depleted in ^{15}N compared to terrestrial atmosphere and meteoritic materials by 40% (Marty et al. 2011). The interesting observation is that although the cosmic abundance of CO is seven times more than that of N_2 in the solar nebula (e.g., Lodders 2003; Asplund et al. 2009), ^{15}N is found to be about seven times more enriched than ^{17}O and ^{18}O in planetary materials relative to the Sun (Marty et al. 2011; McKeegan et al. 2011). The motivation for the present study is to acquire the necessary experimental data to explain the degree of heavy isotope enrichment of N over O in the terrestrial planets relative to the Sun.

2. Need for Branching Ratio Measurements of VUV photodissociation of CO and N$_2$
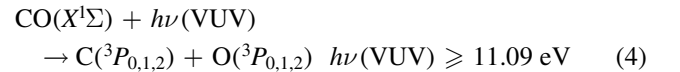
Clayton (2011) suggested that the difference in the heavy isotope enrichment for nitrogen compared to oxygen is attributable to the difference in chemical reactivity of the product atoms formed in different electronic states by the photodissociation of CO and N_2. The differences in chemical reactivity of the photofragment atoms can influence their subsequent trapping efficiencies. In order to provide a quantitative verification of this suggested mechanism, accurate product yields for O and N atoms formed in accessible electronic states, i.e., branching ratio determinations for VUV photodissociation of CO and N_2 are needed.

The $D_0(N_2)$ is 9.7537 ± 0.0011 eV (127.12−0.02/+0.01 nm) (Tang et al. 2005) and thus, there are three accessible energetically allowed dissociation channels (1)–(3), in the energy interval between 9.75–13.60 eV (91.17–127.12 nm):

$$N_2(X^1\Sigma_g^+) + h\nu(\text{VUV})$$

$$\rightarrow N(^4S_{3/2}) + N(^4S_{3/2})$$
$$h\nu(\text{VUV}) \geqslant 9.754 \text{ eV} = 127.1 \text{ nm} \qquad (1)$$

$$\rightarrow N(^4S_{3/2}) + N(^2D_{1/2,3/2})$$
$$h\nu(\text{VUV}) \geqslant 12.13 \text{ eV} = 102.2 \text{ nm} \qquad (2)$$

$$\rightarrow N(^4S_{3/2}) + N(^2P_{1/2,3/2})$$
$$h\nu(\text{VUV}) \geqslant 13.33 \text{ eV} = 93.02 \text{ nm}. \qquad (3)$$

Previous photodissociation studies reported that reaction (1) is negligible (e.g., Helm & Cosby 1989; Walter et al. 1993, 2000). However, these studies involved high rotational levels of excited predissociative states of N_2, whereas low rotational levels are of interest in astronomical environments. Recent work in our laboratory has shown that direct single-photon excitation with a VUV laser from low rotational levels of $N_2(X^1\Sigma_g^+)$ produces only atoms $N(^4S) + N(^2D)$ from reaction (2) 11.09–13.60 eV (91.17–111.78 nm) (Gao et al. 2011b; Pan et al. 2011; Song et al. 2016). This observation is in agreement with the early studies (Helm & Cosby 1989; Walter et al. 1993, 2000) using visible laser excitation of higher rotational levels of the $N_2(a''^1\Sigma_g^+)$ state. The experiments revealed that the branching ratio of the $N(^4S) + N(^2D)$ channel (2) to the $N(^4S) + N(^2P)$ channel (3) is strongly dependent on the energy of the predissociative level involved. For energy lying below 13.91 eV (89.13 nm), the predissociation mostly leads to $N(^4S) + N(^2D)$, while for energy levels above 13.91 eV, the predissociation primarily produces $N(^4S) + N(^2P)$, where $N(^2P)$ radiates quickly to $N(^2D)$ (Walter et al. 1993). Thus, in the VUV range of 9.75–13.60 eV (91.17–127.12 nm) of interest, about 50% each of $N(^4S)$ and $N(^2D)$ are produced by the VUV photodissociation of N_2.

Similarly to N_2, since the $D_0(\text{CO}) = 11.09$ eV (111.78 nm) and the excited $C(^1D)$ and $O(^1D)$ states are higher than the ground $C(^3P)$ and $O(^3P)$ states by 1.2637 and 1.9674 eV (Moore 1993), respectively, there are also three energetically allowed photodissociation product channels, $C(^3P) + O(^3P)$, $C(^1D) + O(^3P)$, and $C(^3P) + O(^1D)$ in the VUV range of 11.09–13.60 eV (91.17–111.78 nm) as shown in reactions (4)–(6).

$$\text{CO}(X^1\Sigma) + h\nu(\text{VUV})$$

$$\rightarrow C(^3P_{0,1,2}) + O(^3P_{0,1,2}) \quad h\nu(\text{VUV}) \geqslant 11.09 \text{ eV} \qquad (4)$$

$$\rightarrow C(^1D_2) + O(^3P_{0,1,2}) \quad h\nu(\text{VUV}) \geqslant 12.35 \text{ eV} \qquad (5)$$

$$\rightarrow C(^3P_{0,1,2}) + O(^1D_2) \quad h\nu(\text{VUV}) \geqslant 13.06 \text{ eV}. \qquad (6)$$

The VUV induced predissociation of $\text{CO}(X^1\Sigma)$ leading to the formation of these product channels has not been examined in detail until recently (e.g., Okazaki et al. 1998, 2001; Gao et al. 2011a, 2012, 2013a, 2013b). In the past, it was assumed that the ground state channel (4) dominates the photodissociation of CO in the VUV region because formation of the triplet dissociation channels (5) and (6) violates the Wigner electron spin conservation rule. Nevertheless, recent studies (Gao et al. 2011a, 2012, 2013a, 2013b) have reported evidence for the formation of the excited $C(^1D) + O(^3P)$ channel (5) by detecting atomic $C(^1D)$.

Excited $O(^1D)$ and $N(^2D)$ atoms are known to be significantly more reactive than their respective ground state $O(^3P)$ and $N(^4S)$ atoms at the same collision energy (e.g., Hsu et al. 1997; Lin & Guo 2008; Zhou et al. 2008). This is partly due to the additional electronic energy of the excited states. By knowing the branching ratios for the accessible product channels from different predissociative rovibronic states of CO and N_2 in the relevant VUV range, it is possible to quantitatively estimate the trapping yields for N and O atoms as described below. Since the branching ratios for photoproduct channels formed by predissociation of N_2 in the energy range of ≈9.75–13.60 eV (91.17–127.1 nm) have been previously determined (Walter et al. 1993, 2000; Gao et al. 2011b; Pan
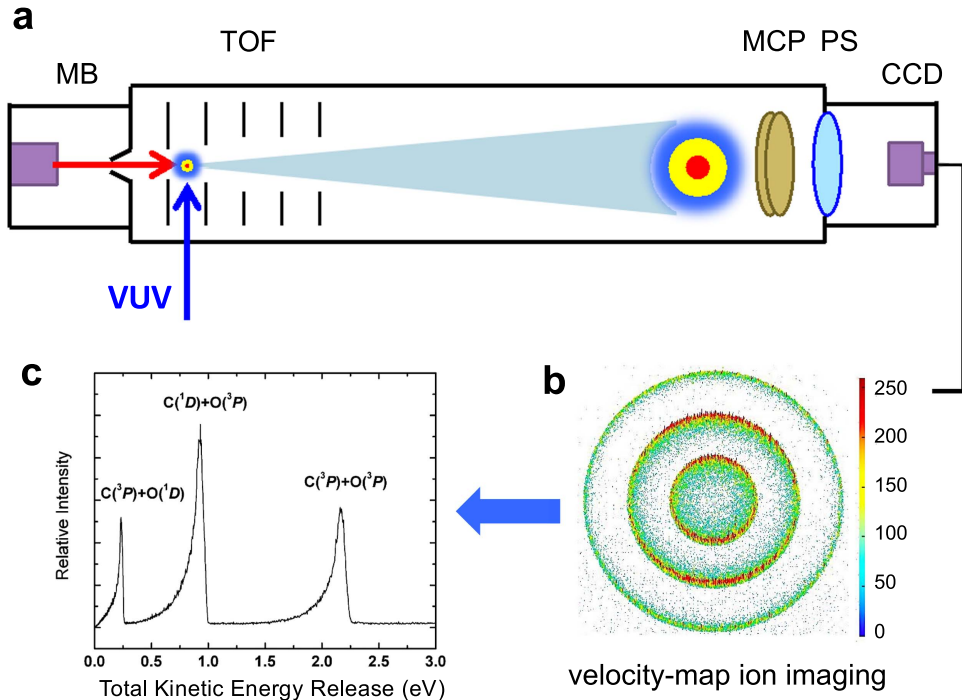
Figure 1. Schematic diagram showing the layout of the VUV laser time-slice velocity-map-imaging-photoion (VMI-PI) apparatus (a). A VUV laser photodissociates CO molecules in the form of a supersonically cooled molecular beam (MB) and ionizes the photofragments C. The time-of-flight (TOF) mass spectrometer is used to detect C^+. The C^+ ions are accelerated and imaged by a set of imaging ion lenses onto the microchannel plate (MCP) ion detector. During the TOF, C^+ ions expand to an ion sphere because C atoms carry part of the center-of-mass kinetic energy (E_{cm}) of C + O photofragments gained from the photodissociation of CO. According to the formula, $E_{cm} = h\nu(VUV) - [D_0 + E(C) + E(O)]$, where $D_0 = 11.09$ eV (Bakker & Parker 2000) is the bond dissociation energy of CO; and $E(C)$ and $E(O)$ represent the internal electronic energies of C and O measured with respect to the respective $C(^3P)$ and $O(^3P)$ ground states. $E(C) = 1.2637$ eV for $C(^1D)$ and $E(O) = 1.9674$ eV for $O(^1D)$ (Moore 1993). Following this formula, C^+ ions corresponding to different dissociation channels have different E_{cm} values. As a result, the ion sphere has multiple layers associated with individual dissociation channels. By gating the MCP at the appropriate time, we detect a middle slice of the C^+ sphere as shown in the time-slice VMI-PI image observed on the phosphor screen (PS) as shown in (b). The VMI-PI image is then converted to the total kinetic energy release (TKER) spectrum as shown in (c). The area of each peak in the TKER spectrum gives the intensity of a dissociation channel. The respective VMI-PI image and its corresponding TKER spectrum depicted in (b) and (c) are observed in the photodissociation of CO excited to the $^1\Pi(v' = 0)$ band at 93.10 nm.

et al. 2011), including our recent work (Gao et al. 2011a; Pan et al. 2011; Song et al. 2016), the key for a quantitative understanding of the different isotope enrichment for nitrogen over oxygen is to determine the branching ratios of product channels, $C(^3P) + O(^3P)$, $C(^1D) + O(^3P)$, and $C(^3P) + O(^1D)$, produced by VUV photodissociation of CO for all 33 bands between 91.17 and 111.78 nm as listed by Visser et al. (2009).

Building on our recent comprehensive studies (Gao et al. 2011a, 2012, 2013a, 2013b), we have completed a detailed investigation of the branching ratios of CO photodissociation induced by VUV excitation in the range of 11.09–13.60 eV (91.17–111.78 nm), using the time-slice velocity-map-imaging-photoion (VMI-PI) technique. The total $O(^1D)$ branching ratio in the CO predissociation is summarized in Table 1 and compared with the total $N(^2D)$ branching ratio in the N_2 predissociation in Table 2. Using these experimental results together with the proposed chemical pathways for nascent atomic oxygen and nitrogen photofragments in the early solar system as described below, we provide an explanation for the observed difference of a factor of 7 in the degree of heavy isotope enrichment of N over O in the terrestrial planets relative to that in the Sun.

3. Experiment

3.1. Branching Ratios of Product Channels from VUV Photodissociation of CO

The branching ratios were measured using the VUV laser photodissociation–photoionization (PD–PI) time-slice VMI-PI

apparatus, which has been described in detail previously (Gao et al. 2011b, 2012, 2013a, 2013b). In this experiment, tunable photodissociation VUV laser radiation was generated by resonance-enhanced four-wave sum-frequency mixing ($2\nu_1 + \nu_2$) using a Xe gas jet as the nonlinear medium, where ν_1 and ν_2 represent the UV and visible laser frequencies, respectively. The ν_1 and ν_2 frequencies are generated by two dye lasers (Lambda Physik, FL3002), which were pumped by the second harmonic output of the same Nd:YAG laser (Spectra Physics PRO-290) operated at 30 Hz. The ν_1 frequency was fixed at 222.568 nm to coincide with the two-photon transition $5p^5(^2P_{1/2})6p^2[1/2](J = 0) \leftarrow 5p^6(^1S_0)$ of Xe. The ν_2 output was generated in the range of 550–650 nm in order to cover the VUV sum-frequency ($2\nu_1 + \nu_2$) output range of 91.17–94.79 nm as required for the present experiment. In addition to the sum-frequency ($2\nu_1 + \nu_2$), the difference-frequency ($2\nu_1 - \nu_2$) and the triple frequency ($3\nu_1$) outputs were also generated when the ν_1 and ν_2 beams were focused into the Xe gas jet. All of these VUV laser beams along with the ν_1 and ν_2 fundamental outputs intersect the supersonically cooled CO molecular beam.

In time-slice VMI measurements, the VUV sum-frequency ($2\nu_1 + \nu_2$) was tuned to a specific rovibronic transition of a predissociative CO absorption band at a time. A high voltage electric field pulse with a width of 40 ns was applied to the front MCP to activate the dual-MCP ion detector at an appropriate delay with respect to the VUV laser pulse, serving

Table 1
Photodissociation Branching Ratios and Cross-sections of CO States from 90.5 to 107.6 nm

Band (a)	(b)	ID	v'	λ_0 (c) (nm)	ν_0 (c) (cm^{-1})	σ (d) (10^{-18} cm^2 nm)	η (e)	O(^1D) (%)	O(^3P) (%)	O(^1D)%×σ×η (10^{-18} cm^2 nm)	O(^3P)%×σ×η (10^{-18} cm^2)	H/H$_2$ line (g)	$\Delta E(\nu_0^{12C^{16}O} - \nu_0^{12C^{18}O})$ (h) (cm^{-1})	O(^1D)%×σ×η (10^{-18} cm^2 nm)	O(^3P)%×σ×η (10^{-18} cm^2 nm)
1A	7A	$^1\Pi$	0	91.27037	109564.58	2.49	1.00	31 (f)	69 (f)	77	172		0.51	small ΔE	small ΔE
1B	7B	(5pσ) $^1\Sigma^+$	1	91.34002	109481.04	1.25	1.00	16 (f)	84 (f)	20	105		52.56	20	105
1C	7C	(5pπ) $^1\Pi$	1	91.34255	109478.00	1.25	1.00	16 (f)	84 (f)	20	105		49.60	20	105
1D	7D	$^1\Sigma^+$	2	91.36678	109448.97	19.90	1.00	26 (f)	74 (f)	509	1481	overlap	103.15	H, H2	H, H2
2A	8A	(6pπ) $^1\Pi$	0	91.57258	109203.00	1.48	1.00	0 (f)	100 (f)	0	148		0.51	small ΔE	small ΔE
2B	8B	(6pσ) $^1\Sigma^+$	0	91.59708	109173.79	5.88	1.00	<5 (f)	>95(f)	29	559		0.51	small ΔE	small ΔE
3	9A	$^1\Pi$	2	91.72721	109018.91	16.90	1.00	57 (f)	43 (f)	965	725	overlap	117.90	H/H$_2$	H/H$_2$
4	9B	(6sσ) $^1\Sigma^+$	0	91.92097	108789.10	2.11	1.00	0	100	0	211		0.51	small ΔE	small ΔE
5	9C	I'(5sσ) $^1\Sigma^+$	1	92.0141	108679.00	2.11	1.00	0	100	0	211		52.56	0	211
6	10	(5dσ)$^1\Sigma^+$	0	92.27561	108371.00	4.76	1.00	<1 (f)	100 (f)	0	476		0.00	small ΔE	small ΔE
7	11	$^1\Sigma^+$	1	92.46309	108151.26	3.90	1.00	<1(f)	100 (f)	0	390		58.26	0	390
8	12	W(3sσ)$^1\Pi$	3	92.58093	108013.60	12.40	1.00	4 (f)	96 (f)	52	1188		179.30	52	1188
9	13	$^1\Pi$	2	92.86575	107682.33	5.10	1.00	5	95	28	482	overlap	96.51	H/H$_2$	H/H$_2$
10	14	$^1\Pi$	2	93.00611	107519.82	4.86	1.00	8	92	37	449	overlap	125.77	H/H$_2$	H/H$_2$
11	15A	$^1\Pi$	0	93.10744	107402.80	4.63	1.00	15	85	68	395	overlap	121.89	H/H$_2$	H/H$_2$
12	15B	(5pπ)$^1\Pi$	0	93.16547	107335.90	9.27	1.00	4	96	37	890	overlap	54.99	H/H$_2$	H/H$_2$
13	15C	(5pσ)$^1\Sigma^+$	0	93.30583	107174.44	16.99	1.00	1	99	14	1685		2.00	small ΔE	small ΔE
14	16	$^1\Sigma^+$	2	93.56638	106876.00	2.92	1.00	3	97	10	282		95.80	10	282
15	17	I(5sσ) $^1\Sigma^+$	0	93.99574	106387.80	16.70	1.00	<1	100	0	1670		19.50	0	1670
16	18	W(3sσ)$^1\Pi$	2	94.11685	106250.90	20.22	1.00	8 (f)	92 (f)	164	1858		58.40	164	1858
17	19	(4dσ)$^1\Sigma^+$	0	94.6286	105676.30	6.04	1.00	0 (f)	100 (f)	0	604	overlap	41.10	H/H$_2$	H/H$_2$
18	20	L(4pπ)$^1\Pi$	1	94.8386	105442.30	2.22	0.99	0	100	0	220		130.80	0	220
19	21	H(4pσ)$^1\Sigma^+$	1	95.00429	105258.40	17.60	1.00	0	100	0	1760		77.50	0	1760
20	22	W(3sσ)$^1\Pi$	1	95.62369	104576.60	10.90	1.00	0	100	0	1090		4.40	small ΔE	small ΔE
21	24	J(4sσ)$^1\Sigma^+$	1	96.43973	103691.70	2.30	1.00	0	100	0	230	overlap	86.20	H/H$_2$	H/H$_2$
22	25	L(4pπ)$^1\Pi$	0	96.83187	103271.78	6.42	0.96	0	100	0	616		22.20	0	616
23	26	L'(3dπ)$^1\Pi$	0	96.88815	103211.80	10.30	1.00	0	100	0	1030		59.20	0	1030
24	27	K(4pσ)$^1\Sigma^+$	0	97.03588	103054.66	17.50	0.99	0	100	0	1733		0.47	small ΔE	small ΔE
25	28	W(3sσ)$^1\Pi$	0	97.26996	102806.66	10.10	0.97	0	100	0	980	overlap	33.95	H/H$_2$	H/H$_2$
26	29	W(3sσ)$^3\Pi$	2	97.73996	102312.30	1.54	1.00	0	100	0	154		107.60	0	154
27	30	F(3dσ)$^1\Sigma^+$	1	98.25914	101771.70	0.41	1.00	0	100	0	41		121.70	0	41
28	31	J(4sσ)$^1\Sigma^+$	0	98.5649	101455.99	13.20	1.00	0	100	0	1320	overlap	26.20	H/H$_2$	H/H$_2$
29	32	G(3dπ)$^1\Pi$	0	98.97952	101031.00	0.40	1.00	0	100	0	40		0.80	small ΔE	small ΔE
30	33	F(3dσ)$^1\Sigma^+$	0	100.25897	99741.70	7.06	1.00	0	100	0	706	overlap	29.40	H/H$_2$	H/H$_2$
31	37	E(3pπ)$^1\Pi$	1	105.17134	95082.94	2.42	0.96	0	100	0	232	overlap	49.27	0	232
32	38	C(3pσ)$^1\Sigma^+$	1	106.3088	94065.59	2.77	0.56	0	100	0	155	overlap	51.18	H/H$_2$	H/H$_2$
33	39	E(3pπ)$^1\Pi$	0	107.60796	92929.93	37.40	0.80	0	100	0	2992		0.37	0	2992
									SUM	2030	27385		SUM	266	13640
										6.9%	93.1%			2.0%	98.0%

Note. (a) Numbering follows van Dishoeck & Black (1988); (b) numbering follows Eidelsberg & Rostas (1990); (c) λ_0 and ν_0 from Ubachs et al. (1994; 2000), Cacciani et al. (2001; 2002), Cacciani & Ubachs (2004), and van Dishoeck & Black 1988; (d) absorption cross-sections σ from Eidelsberg & Rostas (1990) and Eidelsberg et al. (1991); (e) predissociation probability η from Visser et al. (2009); (f) branching ratio from Gao et al. (2011a, 2012, 2013); (g) H/H$_2$ absorption from Baker (2008), van Dishoeck & Black (1988) and Visser et al. (2009); (h) energy difference ΔE between the band centers (ν_0) of $^{12}C^{16}O$ and $^{12}C^{18}O$ from Eidelsberg et al. (1991).

Table 2
Photodissociation Branching Ratios and Cross-sections of N_2 States from 91.17 to 127.12 nm

F (a)	ID	v'	$\lambda_0(^{14}N_2)$ (b) (nm)	$\nu_0(^{14}N_2)$ (b) (cm⁻¹)	$\nu_0(^{14}N^{15}N)$ (c) (cm⁻¹)	σ (d) (10⁻¹⁸ cm² nm)	$N(^2D)$ (e) (%)	$N(^4S)$ (e) (%)	H/H₂ absorption (f)	$\Delta E(\nu_0^{\,14}N_2 - \nu_0^{\,14}N^{15}N)$ (g) (cm⁻¹)	$N(^2D)\% \times \sigma$ (10⁻¹⁸ cm² nm)	$N(^4S)\% \times \sigma$ (10⁻¹⁸ cm² nm)
1	$3s\sigma_g\,\rho_3\,^1\Pi_u$	2	91.2742	109560	NA	136	50	50	Overlap	NA	H/H₂	H/H₂
2	$b\,^1\Pi_u$	11	91.6422	109120	108998	29.4	50	50	Overlap	122	H/H₂	H/H₂
3	$b'\,^1\Sigma_u^+$	7	91.7835	108952	108878	13.6	50	50	Overlap	74	H/H₂	H/H₂
4	$3p\pi_u\,c_3\,^1\Pi_u$	2	92.0022	108693	108625	84.1	50	50		68	4205	4205
5	$3p\sigma_u\,c_4'\,^1\Sigma_u^+$	2	92.1285	108544	108470	9.9	50	50		74	495	495
6	$b\,^1\Pi_u$	10	92.2748	108372	108263	75.1	50	50		109	3755	3755
7	$b'\,^1\Sigma_u^+$	6	92.5934	107999	107937	13.3	50	50		62	665	665
8	$3s\sigma_g\,\rho_3\,^1\Pi_u$ + $b\,^1\Pi_u$	o(1) b(9)	92.9057 92.8954	107636 107648	107607 107545	137	50	50	Overlap	29 103	H/H₂	H/H₂
9	$b'\,^1\Sigma_u^+$	5	93.1741	107326	107277	8.2	50	50	Overlap	49	H/H₂	H/H₂
10	$b\,^1\Pi_u$	8	93.5165	106933	106848	3.6	50	50		85	180	180
11	$b'\,^1\Sigma_u^+$	4	93.7673	106647	106608	14.6	50	50		39	730	730
12	$3p\pi_u\,c_3\,^1\Pi_u$	1	93.8720	106528	106489	303	50	50	Overlap	39	H/H₂	H/H₂
13	$3p\sigma_u\,c_4'\,^1\Sigma_u^+$	1	94.0115	106370	106338	167	50	50		32	8350	8350
14	$b\,^1\Pi_u$	7	94.2409	106111	106045	148	50	50		66	7400	7400
15	$b'\,^1\Sigma_u^+$	3	NA	NA	NA	2.0	50	50		NA	100 (h)	100 (h)
16	$3s\sigma_g\,\rho_3\,^1\Pi_u$	0	94.6226	105683	105664	1.29	50	50	Overlap	19	H/H₂	H/H₂
17	$b\,^1\Pi_u$	6	94.9253	105346	105291	33.1	50	50		55	1655	1655
18	$b'\,^1\Sigma_u^+$	2	NA	NA	NA	0.2	50	50		NA	10 (h)	10 (h)
19	$b\,^1\Pi_u$	5	95.5110	104700	104657	24.6	50	50	Overlap	43	H/H₂	H/H₂
20	$3p\sigma_u\,c_4'\,^1\Sigma_u^+$ + $b'\,^1\Sigma_u^+$	c'(0) b'(1)	95.8561 95.7680	104323 104419	104324 104419	47.7	50	50		−1 0	small ΔE small ΔE	small ΔE small ΔE
21	$3p\pi_u\,c_3\,^1\Pi_u$	0	96.0255	104139	104105	407	50	50		34	20350	20350
22	$b\,^1\Pi_u$ + $b'\,^1\Sigma_u^+$	b(4)+b'(0)	96.5726	103549	103517	490	50	50	Overlap	32	H/H₂	H/H₂
23	$3p\pi_u\,c_3\,^1\Pi_u$	3	97.2157	102864	102841	325	50	50	Overlap	23	H/H₂	H/H₂
24	$b\,^1\Pi_u$	2	97.8933	102152	102140	176	50	50		12	8800	8800
25	$b\,^1\Pi_u$	1	98.5688	101452	101454	42.3	50	50	Overlap	−2	H/H₂	H/H₂
26	$b\,^1\Pi_u$	0	99.1896	100817	100830	21.1	50	50	Overlap	−13	H/H₂	H/H₂
										SUM	56595	56495
											50%	50%

Note. The N_2 photoabsorption and photodissociation in the energy range of 100–127.12 nm are negligible, and thus, are not listed. (a) Band numbering follows Li et al. (2013); (b) λ_0 ($^{14}N_2$) and ν_0 ($^{14}N_2$) from Stark et al. (2005, 2008); (c) ν_0 ($^{14}N^{15}N$) from Heays et al. (2011); (d) absorption cross-sections σ from Li et al. (2013); (e) branching ratio from Helm and Cosby (1989), Walter et al. (2000), and Gao et al. (2011b); (f) H/H₂ absorption from Baker (2008), van Dishoeck & Black (1988) and Visser et al. (2009); (g) energy difference ΔE between the band centers (ν_0) of $^{14}N_2$ and $^{14}N^{15}N$ from Stark et al. (2005, 2008), and Heays et al. (2011); (h) these two bands are considered as efficient N_2 self-shielding bands, though their ΔE between the band centers (ν_0) of $^{14}N_2$ and $^{14}N^{15}N$ are not available.

to time-slice the signal of C^+ ions for 40 ns as they arrived at the MCP ion detector (Figure 1).

The procedures for using the VUV laser PD–PI time-slice VMI-PI apparatus for branching ratio measurements has also been reported previously (Zhou et al. 2006; Gao et al. 2011a, 2011b, 2012, 2013a, 2013b). Briefly, the cold CO sample in the form of a molecular beam was prepared by supersonic expansion of pure CO at a stagnation pressure of 50 PSI and temperature of 298 K through a pulsed valve (Evan-Lavie Model: EL-5-2004; nozzle diameter = 0.2 mm) operated at a repetition rate of 30 Hz. In this experiment, the CO pulsed beam traveled along the central axis of the VMI-PI apparatus and was skimmed by two conical skimmers prior to intersecting the VUV laser perpendicularly in the PD–PI center. The resulting nascent C atomic photofragments in the $C(^3P)$ and $C(^1D)$ states were photoionized by the same VUV laser beam. The C^+ ions thus formed were extracted and focused by a set of VMI ion lenses onto a dual-MCP detector with a diameter of 7.5 cm. The electrons from the MCP detector were accelerated onto a phosphor screen (PS), where the image is recorded by a CCD camera.

Since the threshold energy of reaction (6) is 13.06 eV, any excited vibronic bands located at energies lower than 13.06 eV or wavelengths longer than 94.94 nm cannot produce excited $O(^1D)$. Thus, in order to investigate the $O(^1D)$ production from CO photodissociation in the range of 91.17–111.78 nm, it is only necessary to perform the branching fraction measurement for the $C(^3P) + O(^1D)$ channel of CO predissociation in the region of 91.17–94.79 nm.

3.2. Photofragment Spectra of C and O Atoms from VUV Photodissociation of CO

To confirm that the ground state and excited C and O atoms observed are produced by the predissociation of CO induced by VUV excitation, we have measured the photofragment spectra of $C(^3P)$, $C(^1D)$, $O(^3P)$, and $O(^1D)$ from all relevant CO absorption bands in the VUV range of interest. Since the ionization energy (IE) for the C atom is 11.26 eV (or 110.1 nm), which is lower than the photon energies of the VUV sum-frequency ($2\nu_1 + \nu_2$) laser output, the detection of C atoms in the $C(^3P)$ and $C(^1D)$ states can be readily achieved by photoionization sampling using the same VUV sum-frequency laser beam used for photodissociation of CO. Thus, the photofragment spectrum of C from CO was recorded by measuring the C^+ TOF intensity as a function of VUV sum-frequency using the VMI apparatus.

However, the IE for $O(^3P)$ is 13.62 eV (91.0 nm), and the energy of the VUV used for photodissociation is not high enough to ionize the O atom in its ground state. In order to measure the photofragment spectra of $O(^3P_J)$ and $O(^1D_2)$, we had to equip our setup with another VUV source (Shi 2012). While the first VUV laser (VUV_1) is used to induce photodissociation of CO, the second VUV laser (VUV_2) together with the fundamental UV laser output (ν_1) ionized O atoms produced by VUV_1 photodissociation of CO. In the present measurement of the photofragment spectra of $O(^3P)$ and $O(^1D_2)$ from VUV_1 photodissociation of CO, VUV_2 was set at 107,583.02 cm^{-1} (13.3386 eV) for the Rydberg transition $2s^22p^3(^4S^\circ)7d \leftarrow 2s^22p^4 \ (^3P_2)$, and 106,928.86 cm^{-1} (13.2574 eV) to promote the transition $2s^22p^3(^2D^\circ_{3/2})4s \leftarrow 2s^22p^4 \ (^1D_2)$, respectively.

4. Results and Discussions

4.1. Observation of Atomic $O(^1D)$ from VUV Photodissociation of CO

Due to the high IE of oxygen atoms, their direct quantitative detection as photofragments from VUV photodissociation of CO is difficult (Okazaki et al. 2001). Thus, the O^+ photofragment spectrum of $O(^1D)$ from CO has not been previously reported. With the two-color VUV photodissociation and VUV photoionization scheme (Shi et al. 2012; Gao et al. 2013b) developed in our laboratory, we have recorded for the first time the observation of the atomic $O(^1D)$ produced in CO predissociation. This observation is the evidence of the formation of the triplet dissociation channels (5) and (6), which violates the Wigner electron spin conservation rule.

Figures 2(a) and 1(b) depict the O^+ photofragment spectra of $O(^3P)$ and $O(^1D)$ from CO predissociation recorded from 92.6 to 94.1 nm (or 13.18 to 13.39 eV). In this VUV range, both $O(^1D)$ and $O(^3P)$ were observed from all the excited absorption bands, except for band I $(5s\sigma)^1\Sigma^+(v'=0, \ \lambda_0 = 93.99$ nm). Considering the energetics of CO dissociation and the energies of the CO absorption bands between 91.17 and 111.78 nm (or 11.09 and 13.60 eV), $O(^1D)$ atoms can only be produced from the $C(^3P) + O(^1D)$ channel (6), whereas $O(^3P)$ atoms can result from the $C(^3P) + O(^3P)$ (4) and/or $C(^1D) + O(^3P)$ channels (5). Thus, the $O(^1D)$ photofragment spectrum (Figure 2(b)) represents the relative population of the $C(^3P) + O(^1D)$ channel measured as a function of VUV photodissociation energy. The appearance of both $O(^1D)$ and $O(^3P)$ signals in the same predissociative band reveals the nature of the multichannel dissociation of many excited CO bands: $^1\Sigma^+(v'=2, \lambda_0 = 93.57$ nm), $(5p\sigma)^1\Sigma^+(v'=0, \ \lambda_0 = 93.31$ nm), $(5p\pi)^1\Pi$, $^1\Pi \ (v'=2, \lambda_0 = 93.11$ nm), and $^1\Pi \ (v'=2, \lambda_0 = 93.01$ nm). However, the formation of the triplet dissociation channel $C(^3P_{0,1,2}) + O(^1D_2)$ and the $C(^1D_2) + O(^3P_{0,1,2})$ channels violates the Wigner electron spin conservation rule because the initial photoexcitation of $CO(X^1\Sigma^+)$ is expected to produce an excited singlet state. Therefore, to produce the $O(^1D) + C(^3P)$ products from VUV photodissociation of CO in its ground state necessarily involves curve crossings between the directly excited singlet state and a triplet state that correlates to the triplet product channels.

4.2. Branching Ratios in Predissociation of CO States

In this work, time-slice VMI-PI images of the carbon ion (C^+) were taken for each CO predissociation band observed in the photofragment spectra from 92.6 to 95.0 nm. These images were converted to total kinetic energy release (TKER) spectra to identify the three dissociation channels: $C(^3P) + O(^3P)$, $C(^1D) + O(^3P)$, and $C(^3P) + O(^1D)$. Their branching ratios were measured by integrating the areas under the corresponding peaks in the TKER spectra, and then calibrating the areas with the corresponding photoionization cross-sections of $C(^3P)$ and $C(^1D)$. The photoionization cross-sections of $C(^1D)$ that we applied to calibrate the TKER spectra are listed in Table 3. As an example, Figures 1(b) and (c) are the time-slice VMI-PI images of the $^1\Pi$ state at 93.10 nm and its TKER spectrum, respectively. Each ring in the image represents a dissociation channel, corresponding to a peak in the TKER spectrum. The inner ring consists of C^+ ions formed by the
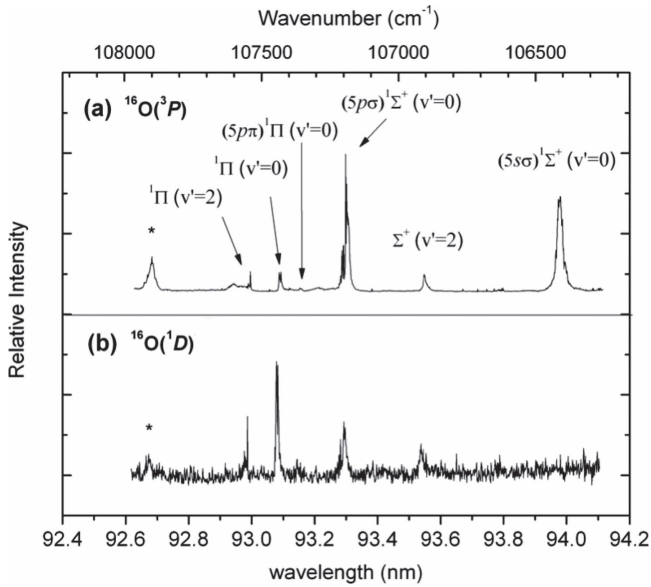
Figure 2. O$^+$ photofragment spectra of O(^1D) and O(^3P) from CO in the VUV range of 92.6–94.1 nm (106,270–108,000 cm^{-1}). The signal-to-noise ratios of the O$^+$ photofragment spectrum of (a) O(^3P) are better than that of (b) O(^1D) primarily due to the fact that the branching yield of C(^3P) + O(^3P) is higher than that of C(^3P) + O(^1D). The peaks at 92.69 nm marked by asterisks (*) in (a) and (b) were not due to CO photodissociation because the C$^+$ VMI-PI taken at this wavelength showed no ring structure. They are likely due to predissociation of a small CO$_2$ impurity. CO$_2$ has a strong absorption in this region (Nakata et al. 1965).

Table 3
Photoionization Cross-sections of C(^1D) Used to Calibrate the TKER Spectra of CO

| Band | | ID | v' | λ_0 (c) | Photoionization |
(a)	(b)			(nm)	σC(^1D) (d) (10^{-18} cm^2)
9	13	$^1\Pi$	2	92.86575	23
10	14	$^1\Pi$	2	93.00611	23
11	15A	$^1\Pi$	0	93.10744	23
12	15B	(5pπ) $^1\Pi$	0	93.16547	24
13	15C	(5pσ) $^1\Sigma^+$	0	93.30583	24
14	16	$^1\Sigma^+$	2	93.56638	25
15	17	I(5sσ) $^1\Sigma^+$	0	93.99574	26
16	18	W(3sσ) $^1\Pi$	2	94.11685	29 (e)
17	19	(4dσ) $^1\Sigma^+$	0	94.6286	26

Note. (a) Band numbering follows van Dishoeck & Black (1988); (b) numbering follows Eidelsberg & Rostas (1990); (c) λ_0 and ν_0 from Ubachs et al. (1994, 2000), Cacciani et al. (2001, 2002), Cacciani & Ubachs (2004), and van Dishoeck & Black (1988); (d) photoionization cross-sections σ of C(^1D) from Cantù et al. 1981; (e) photoionization cross-sections σ of C(^1D) from Gao et al. (2013a), and Burke & Taylor (1979).

photoionization of C(^3P) atoms associated with the C(^3P) + O(^1D) channel (6) produced with the lowest kinetic energy in CO photodissociation. Based on the conservation of energy, we have

$$h\nu(\text{VUV}) = D_0 + E_{cm} + E(\text{C}) + E(\text{O}), \quad (7)$$

where $h\nu$(VUV) is the energy of the VUV sum-frequency ($2\nu_1 + \nu_2$) used for photoexcitation; D_0(CO) = 11.09 eV (Bakker & Parker 2000); E_{cm} is the center-of-mass kinetic energy of the photofragments, C and O atoms associated with a specific product channel; and E(C) and E(O) represent the internal electronic energies of C and O measured with respect to the respective C(^3P) and O(^3P) ground states. Here, E(C) = 1.2637 eV for C(^1D) and E(O) = 1.9674 eV for O(^1D) (Moore 1993).

Table 1 summarizes the branching ratio data from 91.17 nm (13.60 eV) to 111.78 nm (11.09 eV) weighted by their respective absorption cross-sections (Letzelter et al. 1987; Eidelsberg & Rostas 1990; Eidelsberg et al. 1991; Eikema et al. 1994) and predissociation probability (Visser et al. 2009). At a longer wavelength above 105 nm, the CO molecule fluoresces, but at these wavelengths no O(^1D) is produced since this is below the thermodynamic threshold that produces this excited atom via reaction (6), and the fact that some of the CO does not dissociate is taken care of in the quantum yield, η (Visser et al. 2009). By summing up branching ratios of all the predissociative states, we found the respective total yields of about 6.9% and 93.1% for O(^1D) and O(^3P) atoms produced by CO photodissociation. However, the contributions of some of the predissociative bands are expected to be negligible either due to shielding by H and H$_2$ in the solar nebula or mutual shielding of CO. Lines at 91.37, 91.73, 92.87, 93.01, 93.11,

93.17, 94.63, 96.44, 97.27, 98.56, and 106.31 nm are found to overlap with H and H$_2$ absorption (e.g., van Dishoeck & Black 1988; Baker 2008; Visser et al. 2009). Bands at 91.57, 91.60, 92.28, 95.62, 97.03, and 98.98 nm would have no appreciable CO self-shielding effects because the absorption lines of C^{16}O, C^{17}O, and C^{18}O are too close to each other (Eidelsberg et al. 1991; Warin et al. 1996). After removing these lines, we find that the cumulative O(^1D) percentage of total atomic oxygen from CO photodissociation is reduced to 2.0%.

For comparison, Table 2 summarizes the branching ratios in N$_2$ photodissociation from 91.17 nm (13.60 eV) to 127.12 nm (9.75 eV) weighted by their respective photodissociation cross-sections (Li et al. 2013). This table shows that 50% of N atoms are formed in the excited N(^2D) state in this VUV range relevant to N$_2$ self-shielding (Helm & Cosby 1989; Walter et al. 1993, 2000; Tang et al. 2005; Gao et al. 2011b; Pan et al. 2011).

Thus, the metastable production of N(^2D) from N$_2$ is $50/2.0 = 25$ times greater than that of O(^1D) from CO. This suggests that atomic oxygen photofragments are less reactive on the whole than atomic nitrogen photofragments in the subsequent trapping reactions, so that the oxygen isotope fractionation from self-shielding would be less efficiently expressed into planetary materials than that of nitrogen isotopes. We show that only the excited O(^1D) and N(^2D) atoms, via reactions with H$_2$, help to lock in the isotopic signature from self-shielding. The excited O(^1D) and N(^2D) atoms are trapped quantitatively within their radiative lifetime by hydrogenation reactions, whereas the reaction rate for the ground states O(^3P) (98%) and N(^4S) (50%) in comparison are many orders of magnitude slower (Table 4).

4.3. Hydrogenation of O(^1D) and N(^2D) atoms

The isotopic ratios of oxygen and nitrogen can only be affected by self-shielding if the atoms that are formed by predissociation of N$_2$ and CO react so that they are trapped in stable compounds. The ground state atoms, O($^3P_{0,1,2}$) and

Table 4
The Rate Constants of Reactions of Excited O (^1D) and N (^2D), Ground State O(^3P) and N(^4S) with H$_2$ at 50, 300, and 1500 K

Reaction	A (cm^3 molec^{-1} s^{-1})	E_a/R (K)	k_{50}[a] (cm^3 molec^{-1} s^{-1})	k_{300} (cm^3 molec^{-1} s^{-1})	k_{1500}[a] (cm^3 molec^{-1} s^{-1})
O(^3P) + H$_2$→OH + H	1.6×10^{-11} (a)	4480 (a)	2.0×10^{-50}	5.2×10^{-18}	8.1×10^{-13}
O(^1D) + H$_2$→OH + H	1.5×10^{-10} (b)	0 (b)	1.5×10^{-10}	1.5×10^{-10}	1.5×10^{-10}
N(^4S) + H$_2$→NH + H	2.7×10^{-10} (c)	12650(c)	3.6×10^{-120}	1.3×10^{-28}	5.9×10^{-14}
N(^2D) + H$_2$→NH + H	4.6×10^{-11} (d)	878 (d)	1.1×10^{-18}	2.5×10^{-12}	2.6×10^{-11}

Note.
[a] k_{50} and k_{1500} are calculated reaction rate constants, whereas k_{300} is based on laboratory measurements at room temperature.
References. (a) Han et al. (2000), Baulch et al. (1982), (b) Blitz et al. (2004), (c) Davidson & Hanson (1990), (d) Suzuki et al. (1993).

N($^4S_{3/2}$) do not react very quickly with hydrogen, so it is only the excited metastable atoms that undergo these trapping reactions that ultimately lead to molecules like H$_2$O and NH$_3$, which are among the most common molecules in the protoplanetary disk (Clayton 2011).

As pointed out earlier, the photodissociation reactions (1) through (3) produce the metastable N($^2P_{1/2,3/2}$), and N($^2D_{1/2,3/2}$) through spin-forbidden reactions, but the experiments do not distinguish the branching between the spin–orbit states of these atoms. The reaction stoichiometry of (1) through (3) determines that the sum of both spin–orbit states of the N(^2P) and N(^2D) is 50% of all N atoms. The radiative transition from the (^2P) states to the intermediate ^2D states is so fast (Kramida et al. 2015) that 95% of the ^2P atoms will radiate to the ^2D state. Once the ^2P atoms are in the ^2D state, the radiative lifetime of the N($^2D_{3/2}$) state is 49,300 s, whereas it is 132,000 s for the N($^2D_{5/2}$) state. Because the radiative lifetime of the N($^2D_{3/2}$) is so much shorter than the radiative lifetime of the N($^2D_{5/2}$) state, for self-shielding we should consider these two spin–orbit states separately in calculating what fraction of the excited N(^2D_J) atoms will react in a particular region of the protosolar nebula or astronomical system. Once this is done, we can determine what region of a particular astronomical system will be affected if photodissociation produces one or more of the nitrogen spin–orbit states.

The photoproduct O and N atoms in their excited states O(^1D) and N(^2D) can react efficiently with H$_2$ within their radiative lifetimes (Kramida et al. 2015). By comparing the reaction rates of O(^1D), O(^3P), N(^2D), and N(^4S) with other abundant radicals and molecules in the astrophysical environment, we can obtain a general picture of the reaction pathways of oxygen and nitrogen atoms in the solar nebula. In the following sections, we will discuss the activation energies, reaction rates, and yields of reactions involving atomic O and N in their ground and excited states.

A hydrogenation reaction in the form of X + H$_2$ → XH + H in interstellar space can be considered as a pseudo-first-order reaction, because the concentration of the hydrogen molecule [H$_2$] can be considered a constant throughout the reaction, for which the differential form of the rate law is
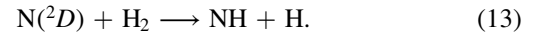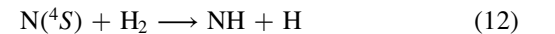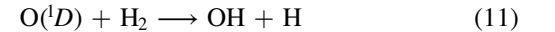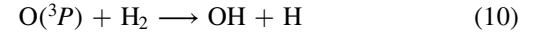
$$\frac{-d[\mathrm{X}]}{dt} = k[\mathrm{X}][\mathrm{H}_2]. \tag{8}$$

Here, k is the rate constant, which is assumed to have the Arrhenius form

$$k = A \exp\left(-\frac{E_a}{RT}\right), \tag{9}$$

where A is the pre-exponential or frequency factor, which is characteristic of the reaction, and E_a is the activation energy, i.e., the energy barrier of the reaction. A reaction can occur when the collision energy of the reactants are equal to or higher than the activation energy. The Boltzmann factor $\exp(-E_a/\mathrm{RT})$ can be interpreted as the fraction of collisions with translational energy greater than E_a at a temperature T.

In this work, the possible reactants are 98.0% O(^3P) and 2.0% O(^1D) from CO photodissociation, and 50% N(^4S) and 50% N(^2D) from N$_2$ photodissociation. The first (and rate-limiting) step in trapping is most likely reactions with the abundant molecular hydrogen, H$_2$:

$$\mathrm{O}(^3P) + \mathrm{H}_2 \longrightarrow \mathrm{OH} + \mathrm{H} \tag{10}$$

$$\mathrm{O}(^1D) + \mathrm{H}_2 \longrightarrow \mathrm{OH} + \mathrm{H} \tag{11}$$

$$\mathrm{N}(^4S) + \mathrm{H}_2 \longrightarrow \mathrm{NH} + \mathrm{H} \tag{12}$$

$$\mathrm{N}(^2D) + \mathrm{H}_2 \longrightarrow \mathrm{NH} + \mathrm{H}. \tag{13}$$

The E_a for the reaction O(^3P) + H$_2$ (10) was measured to be 0.39 eV (E_a/R = 4480 K) (Han et al. 2000). This value agrees with the rate constant $1.6 \times 10^{-11}\exp(-4570/T)$ cm^3 molec^{-1} s^{-1} evaluated by the IUPAC CODATA Task Group on Chemical Kinetics (Baulch et al. 1982) and the recent theoretical calculations (Lahankar et al. 2013). The experimental temperature-independent reaction constant of $(1.5 \pm 0.1) \times 10^{-10}$ cm^3 molec^{-1} s^{-1} (Blitz et al. 2004) for reaction (11), which is a barrierless reaction, is several orders of magnitude greater than that for reaction (10) at low temperatures (see Table 4). Previous chemical dynamics studies (Hsu et al. 1997; Lin & Guo 2008) indicate that reaction (10) proceeds by H-abstraction via a collinear geometry, whereas reaction (11) favors an insertion mechanism via the formation of an activated collision complex H$_2$O*. None of these reactions tell us how the spin–orbit state affects the rate constant for the reaction, so we will assume that the rate constant is independent of this factor.

Based on the conservation of energy and linear momentum for the dissociation reaction of (4), O(^3P) atoms for reaction (10) can have the range of kinetic energies (E_k's) from 0.00–1.07 eV, depending on the energy of the predissociation band excited. The maximum E_k of 1.07 eV corresponds to VUV$_1$ excitation of the highest energy band at 13.58 eV as listed in Table 1. Assuming that the H$_2$ reactant molecules are at low ambient temperatures, the latter maximum E_k value corresponds to the maximum E_{cm} value of 0.119 eV (11.5 kJ/mol) for the O(^3P) and H$_2$ colliding pair. Since this is well below the energy barrier of 0.39 eV (Han et al. 2000) for reaction (10), its role as a trapping reaction should be

negligible. Because of the significantly higher rate constant for the $O(^1D)$ + H_2 reaction than that for the $O(^3P)$ + H_2 reaction (Table 4), we conclude that only reaction (11) is needed to be considered as a trapping reaction.

Reaction rate constants for (12) [$N(^4S)$ + H_2] and (13) [$N(^2D)$ + H_2] have been experimentally determined to be 2.7×10^{-10} exp($-12650/T$) and 4.6×10^{-11} exp($-878/T$) cm^3 molec^{-1} s^{-1}, respectively (Davidson & Hanson 1990; Suzuki et al. 1993), with the activation barriers of 1.1 and 0.076 eV for $N(^4S)$ + H_2 (12), and $N(^2D)$ + H_2 (13), respectively. These values are consistent with theoretical predictions (Pascual et al. 2002; Zhou et al. 2008; Zhai & Han 2011). Only the $N(^4S)$ + $N(^2D)$ channel (reaction (2)) was observed in this VUV photodissociation energy range between 11.09 and 13.60 eV (Gao et al. 2011b; Pan et al. 2011; Song et al. 2016). Considering that the highest energy band (Band 1 in Table 2) has the energy of 13.58 eV (91.27 nm), the formation of $N(^4S)$ and $N(^2D)$ by channel (2) at 12.13 eV has the maximum energy release of 1.45 eV. Since the two photofragment atoms have the same mass, each of $N(^4S)$ and $N(^2D)$ is expected to carry a E_k of 0.73 eV. For a H_2 reactant sample at low temperatures, this E_k for $N(^4S)$ [or $N(^2D)$] corresponds to a E_{cm} of 0.09 eV for the collision of H_2 and $N(^4S)$ [or $N(^2D)$]. On the basis of the significantly higher activation barrier of 1.1 eV for the ground state reaction (12) compared to the maximum E_{cm} of 0.09 eV, we can confidently ignore it as a trapping reaction. As shown in Table 4, the experimental rate constant at 300 K, $k_{300} = 1.3 \times 10^{-28}$ cm^3 molec^{-1} s^{-1} for reaction (12) is negligible compared to that of $k_{300} = 2.5 \times 10^{-12}$ cm^3 molec^{-1} s^{-1} for reaction (13) (Table 4). Based on the discussion above, it is safe to conclude that only $O(^1D)$ and $N(^2D)$ atoms can be trapped efficiently by their reactions with gaseous H_2 as shown by reactions (11) and (13).

The discussions above proved that the ground state $O(^3P)$ and $N(^4S)$ atoms have little reactivity toward gas phase H_2 in low temperature environments, while metastable $O(^1D)$ and $N(^2D)$ atoms can be terminated efficiently by H_2 (Table 4). However, the ground state $O(^3P)$ and $N(^4S)$ can still be hydrogenated on grain surfaces through reactions $O(^3P)$ + H + grain $\rightarrow$ OH + grain, and $N(^4S)$ + H + grain $\rightarrow$ NH + grain (Hasegawa et al. 1992). These reactions of H and O on grains are suggested to be the dominant pathway for trapping (ground state) O atoms produced from CO photolysis in Lyons and Young's report (2005) and Yurimoto and Kuramoto's report (2004). Considering the low number density of the grains in the molecular clouds, the trapping rates of $O(^3P)$ and $N(^4S)$ atoms should be much slower than the trapping rates of $O(^1D)$ and $N(^2D)$ atoms in the gas phase (Hasegawa et al. 1992; Willacy et al. 1998). However, since the energy barrier of the gas phase $O(^3P)$ hydrogenation is moderate, the reaction can take place efficiently at locations with relatively high temperature in the solar nebula (Table 4, k_{300}, k_{1500}).

4.4. Lifetime, Branching Ratio, and Trapping Yield

From the last section, we know that only atomic oxygen and nitrogen at excited states could be efficiently trapped to OH and NH. In this section, we will calculate the trapping yields as a function of H_2 number densities. In addition to H_2 number densities and reaction rate constants, another crucial parameter that affects the reaction rate is the natural radiative lifetime of an excited state. The relaxation of $O(^1D)$ and $N(^2D)$ to the $O(^3P)$ and $N(^4S)$ ground states by emission of a photon in a finite amount of time can result in a significant decrease

in chemical reactivity. Therefore, we also need to take into account the finite lifetimes of $O(^1D)$ and $N(^2D)$ along with their bimolecular reactions with H_2 to obtain the reaction yields.

The $O(^1D_2)$ lifetimes for radiation to the ground electronic $O(^3P_2)$ and $O(^3P_1)$ are 177 and 544 s, respectfully. Radiation to the $O(^3P_0)$ is a thousand times slower and has been neglected (Kramida et al. 2015). The radiative reactions for these two excited atoms can be written as processes (14):

$$O(^1D_2) \rightarrow O(^3P_2) + h\nu \tag{14a}$$

$$O(^1D_2) \rightarrow O(^3P_1) + h\nu. \tag{14b}$$
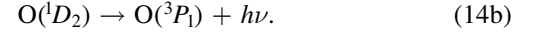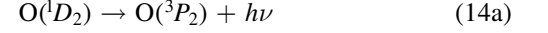
Using these reactions along with the earlier reactions (11), we can write the following equations for the time dependence of $O(^1D)$:

$$d[O(^1D_2)]/dt = -\{(1/\tau_{14a} + 1/\tau_{14b})/2 + k_{11}[H_2]\}[O(^1D_2)] \tag{15}$$

Equation (15) can be integrated to yield the time dependence of the $O(^1D)$ concentration,

$$[O(1D_2)]_t = [O(^1D_2)]_0 \exp -\{(1/\tau_{14a} + 1/\tau_{14b})/2 + k_{11}[H_2]\} \tag{16}$$

The radiative lifetimes for the two spin–orbit components of $N(^2D_{3/2,5/2})$ are 49,100 and 132,000 s for the 3/2 and 5/2 spin–orbit states. Treating the nitrogen atoms similar to the oxygen atoms:

$$N(^2D_{3/2}) \rightarrow N(^4S^0_{3/2}) + h\nu \tag{17a}$$

$$N(^2D_{5/2}) \rightarrow N(^4S^0_{3/2}) + h\nu \tag{17b}$$
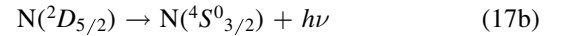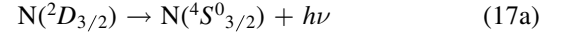
$$d[N(^2D_{3/2}) + N(^2D_{5/2})]/dt = d[N(^2D_{3/2,5/2})]/dt$$
$$= -\{(1/\tau_{17a} + 1/\tau_{17b})/2 + k_{13}[H_2]\}[N(^2D_{3/2,5/2})] \tag{18}$$

$$[N(^2D_{3/2,5/2})]_t = [N(^2D_{3/2,5/2})]_0 \exp$$
$$-\{(1/\tau_{17a} + 1/\tau_{17b})/2 + k_{13}[H_2]\}t \tag{19}$$

where we have explicitly assumed that the reactivity of the 3/2 and 5/2 states are the same. This is likely since they are only 8.3 cm^{-1} apart in energy.

Both $O(^1D)$ and $N(^2D)$ can be quenched effectively by collisions with other molecules. The reaction rates of quenching by Xe, O_2, CO, N_2, and NO were previously measured (Okabe 1978). The quenching rate constants at room temperature for $O(^1D)$ are on the order of 10^{-10} cm^3 molec^{-1} s^{-1} (Davidson et al. 1976), while the quenching rate constants for $N(^2D)$ vary from 10^{-12} to 10^{-10} cm^3 molec^{-1} s^{-1} (Husain et al. 1974). These quenching rate constants are similar to or less than the hydrogenation reaction rate constants of $O(^1D)$ and $N(^2D)$ at the same temperature (Table 4). However, the number density of H_2 is many orders of magnitude higher than those quenching molecules (Allen & Bobinson 1977). Therefore, the quenching reactions of $O(^1D)$ and $N(^2D)$ with other molecules cannot compete with the hydrogenation reactions. Within the finite lifetime τ of the excited $O(^1D)$ or $N(^2D)$ states, the reaction yield is

$$\frac{[X]_0 - [X]_t}{[X]_0} = 1 - e^{-\{(\tau)^{-1} + k[H_2]\}t}. \tag{20}$$

Table 5
Simulated Trapping Yields of Atomic N and O in Solar Nebula

Radial Distance (au)	$[H_2]$ (cm^{-3})	T (K)	k N(^2D) + H$_2$ (cm^3 molec^{-1} s^{-1})	k O(^1D) + H$_2$ (cm^3 molec^{-1} s^{-1})	Trapping Yield[a] N:O N($^2D_{3/2}$)	Trapping Yield[a] N:O N($^2D_{5/2}$)	Trapping Yield[a] N:O 1/2 N($^2D_{3/2}$) 1/2 N($^2D_{5/2}$)
0.1	1.5×10^{16}	1500	2.6×10^{-11}	1.5×10^{-10}	25	25	25
1	7.5×10^{13}	600	1.1×10^{-11}	1.5×10^{-10}	25	25	25
5	7.5×10^{12}	180	3.5×10^{-13}	1.5×10^{-10}	25	25	25
7	6.0×10^{12}	100	7.1×10^{-15}	1.5×10^{-10}	25	25	25
9	4.5×10^{12}	60	2.0×10^{-17}	1.5×10^{-10}	25	25	25
10	4.5×10^{12}	50	1.1×10^{-18}	1.5×10^{-10}	20	25	22
100[b]	5.3×10^{11}	10	3.4×10^{-49}	1.5×10^{-10}	≈ 0	≈ 0	≈ 0

Notes. The $[H_2]$ and temperatures are from Willacy et al. (1998).
[a] The trapping yields are calculated using Equations (23) and (24), except for the condition at 100 au. The reaction times used for N($^2D_{3/2}$) + H$_2$ and N($^2D_{5/2}$) + H$_2$ are 49,100 s and 132,000 s respectively.
[b] The hydrogenation of N(^2D) is negligible at 100 au because the reaction rate constant of N(^2D) + H$_2$, $k[H_2] = 1.7 \times 10^{-37}$ s^{-1} is much smaller than the radiative relaxation rate constants of N($^2D_{3/2}$) and N($^2D_{5/2}$), which are $1/\tau_{14a} = 2.0 \times 10^{-5}$ s^{-1} and $1/\tau_{14b} = 7.6 \times 10^{-6}$ s^{-1}.

For reactions O(^1D) + H$_2$ (16) and N(^2D) + H$_2$ (19), the respective reaction yields after one lifetime can be calculated as

$$\frac{[O(^1D)]_0 - [O(^1D)]_{\tau_{14}}}{[O(^1D)]_0} = 1 - e^{-(1+k_{11}[H_2]\tau_{14})} \quad (21)$$

$$\frac{[N(^2D)]_0 - [N(^2D)]_{\tau_{17}}}{[N(^2D)]_0} = 1 - e^{-(1+k_{13}[H_2]\tau_{17})}, \quad (22)$$

when the timescale of hydrogenation is smaller than the lifetime of the O(^1D) or N(^2D) states, $(1/k_{11}[H_2]) < \tau_{14}$ and $(1/k_{13}[H_2]) < \tau_{17}$.

The trapping yields of O and N atoms can be calculated as the reaction yields for reactions O(^1D) + H$_2$ (21) and N(^2D) + H$_2$ (22) scaled by the fractional yields of [O(^1D)]/[O] (2.0%) and [N(^2D)]/[N] (50%) from CO and N$_2$ predissociation, respectively, as expressed by Equations (23) and (24). These equations have taken into account the effect of temperature T, $[H_2]$, radiative lifetimes (τ's) for O(^1D) and N(^2D), and the product branching ratios of CO and N$_2$ predissociation in the relevant VUV energy range

Trapping yield for O = Reaction yield [O(^1D) + H$_2$]

$$\times \frac{[O(^1D)]}{[O]} \quad (23)$$

Trapping yield for N = Reaction yield [N(^2D) + H$_2$]

$$\times \frac{[N(^2D)]}{[N]}. \quad (24)$$

The next question to ask is which parameter limits the trapping yields? This depends on the astrophysical environment. Here we use the solar nebula as an example to demonstrate the trapping yields of O and N atoms from CO and N$_2$ predissociation.

We use the solar nebula model of Willacy et al. (1998) to set the gas number density and temperature as a function of the radial distance from the Sun, and assumed that 75% of the gas number density is contributed by hydrogen molecules (Lodders 2003). A comparison of our simulated trapping yields of O and N atoms from predissociation in the solar nebula is summarized in Table 5. Since the ratio of N($^2D_{3/2}$) to N($^2D_{5/2}$) from photodissociation of N$_2$ is unknown, the trapping yields are calculated in three conditions: (1) all N(^2D) atoms at the $^2D_{3/2}$

state; (2) all N(^2D) atoms are at the $^2D_{5/2}$ state; (3) half of N(^2D) atoms are at the $^2D_{3/2}$ state and the other half are at the $^2D_{5/2}$ state. In any condition, the trapping yields of O and N at the locations with a radial distance of less than 9 astronomical unit (au) are limited by excited-state branching in CO and N$_2$ predissociation (2.0% O(^1D), 50.0% N(^2D) respectively), because O(^1D) and N(^2D) are trapped into OH and NH quantitatively in the solar nebula with a very high number density of H$_2$, whereas O(^3P) and N(^4S) hardly react with H$_2$. This results in a constant factor of 25.0 in trapping yields of atomic N to O.

Recent chemical imaging of TW Hya, an analog of the early solar nebula, suggests that the CO snowline is located at $\sim$30 au, whereas the N$_2$ snowline extends to 140–150 au (Qi et al. 2013). Although TW Hya is a K6 star, less luminous than the Sun, the effect is still the same. Beyond the CO snowline, the CO would freeze and as a result the photodissociation of CO is necessarily quenched, whereas N$_2$ dissociation would, in principle, continue much farther out, although both gas number density and photon flux drop significantly, scaling with heliocentric distance R (au) as $1 \times 10^{14} R^{-1.45}$ (for hydrogen molecules, Zhai & Han 2011) and R^{-2}, respectively. Furthermore, gaseous N$_2$ beyond the CO snowline may participate in ion-molecules reactions that cause very large ^{15}N enrichments, as described by Rodgers & Charnley (2008). These are significant factors that would contribute to the observed enrichment of rare N isotopes over those of oxygen isotopes. Therefore, the trapping yields of atomic N to O may be bigger than 50.

5. Summary

CO only carries $\sim$50% of the oxygen budget in the solar nebula (Young 2007). The fraction of oxygen bound in water is $\sim$33% (Young 2007) and the remaining $\sim$17% is in solid materials (e.g., Wiens et al. 1999; Lodders 2003; Young 2007; Asplund et al. 2009; Yin et al. 2009; Krot et al. 2010). In contrast, the fraction of nitrogen bound as N$_2$ in the gas phase would dominate in the solar nebula (Qi et al. 2003; Willacy 2007; Willacy & Woods 2009), while the N bound in solid material is likely to be <1%. As a result, the enrichment of rare isotopes of oxygen due to self-shielding CO in the gas phase is likely to be diluted significantly in the meteoritic records by mixing with the remaining $\sim$50% of the oxygen, which is

bound in water and solid materials. These materials would initially contain oxygen of solar isotopic composition. This COSS dilution was modeled by Lyons & Young (2005). Because nebular nitrogen consists essentially entirely of N_2, there is no equivalent dilution for nitrogen. Consequently, the ratio of enrichment of rare isotope of nitrogen to those of oxygen in the terrestrial planets is expected to double minimally, to >50.

The principle governing the self-shielding model is that the Beer–Lambert law gives rise to the mass independent, but abundance dependent isotopic effect. The Beer–Lambert equation is $\ln(I_o/I) = nl\sigma$, where σ is the absorption cross-section of the gas, and I_o and I represent the respective VUV intensities before and after passing through the gas column with a length of l and number density of n. If the isotope ratio is expressed with the δ-value, e.g., $\delta^{18}O = [(^{18}O/^{16}O)/(^{18}O/^{16}O)_0-1] \times 1000 = [(^{16}O/^{18}O)_0/(^{16}O/^{18}O)-1] \times 1000$, where $(^{18}O/^{16}O)_0$ is the initial isotopic ratio, we will find that $\delta^{18}O$ is proportional to $e^{n_{C16O}l\sigma_{C16O}} - 1$, in the cases when ^{16}O is largely attenuated/shielded at the cloud surface and ^{18}O is not (i.e., $^{18}O = {}^{18}O_o$). Similarly, $\delta^{17}O$ and $\delta^{15}N$ is proportional to $e^{n_{C16O}\sigma_{C16O}} - 1$ and $e^{n_{14N2}l\sigma_{14N2}} - 1$, respectively. However, the observed isotope ratio in compounds (e.g., water) is not only affected by self-shielding but also scaled by the trapping yields of O and N atoms. For a parcel of gas and dust in the solar nebula undergoing self-shielding in the line of sight of incoming VUV, considering trapping yields for the excited percentage of $O(^1D)$ and $N(^2D)$, H_2 shielding, mutual shielding (Tables 1 and 2), and CO dilution over N_2, the cross-section σ in the expression of δ-value needs to be replaced by the effective cross-section σ^*. The effective cross-section for O is the total O (1D %) $\times$ σ in Table 1: the effective cross-section for N is two times the total N (2D %) $\times$ σ in Table 2. Based on our experimental results and discussion, we obtained the effective integrated $\sigma^*(^{14}N_2)/\sigma^*(C^{12}O)$ value of >50. However, the cosmic number density of $n(N_2)$ is seven times less than that of $n(CO)$ in the solar nebula (Lodders 2003; Asplund et al. 2009), resulting in $n(^{14}N_2)/n(C^{12}O) = 1/7$. Therefore, $n(^{14}N_2)l\sigma^*(^{14}N_2) : n(C^{12}O)l\sigma^*(C^{12}O) > 50/7 = 7.1$. The overall observed isotopic effect of N should be significantly bigger than that of O. This is a lower limit considering that the CO snowline is located at $\sim$30 au, whereas the N_2 snowline extends to 140–150 au (Qi et al. 2013). Therefore, N_2 self-shielding can proceed in the outer solar system beyond the snowline of CO, and inward transport of materials from the outer solar system would raise the difference between the isotopic effects of N and O.

Compared to the *Genesis* mission observation that rare isotope of ^{15}N in terrestrial planets and meteorites is $\sim$7 times more enriched than ^{17}O and ^{18}O relative to the Sun (Marty et al. 2011; McKeegan et al. 2011), our analyses lend qualitative support to the "trapping reaction" hypothesis suggested by Clayton (2011), and provide a possible explanation of the difference between ^{15}N and $^{17,18}O$ enrichment in the planetary materials compared to the Sun observed by the *Genesis* mission.

ORCID iDs

Xiaoyu Shi ⓘ https://orcid.org/0000-0002-9634-2659
Qing-Zhu Yin ⓘ https://orcid.org/0000-0002-4445-5096
Cheuk-Yiu Ng ⓘ https://orcid.org/0000-0003-4425-5307

References

Ajello, J., James, G., Franklin, B., & Shemansky, D. 1989, PhRvA, 40, 3524
Allen, M., & Bobinson, G. W. 1977, ApJ, 212, 395
Asplund, M., Grevesse, N., Sauval, A. J., & Scott, P. 2009, ARA&A, 47, 481
Baker, J. 2008, Natl. Inst. Stand. Technol. Technical Note, 1612, 8, http://nvlpubs.nist.gov/nistpubs/Legacy/TN/nbstechnicalnote1612.pdf
Bakker, B. L. G., & Parker, D. H. 2000, CPL, 330, 293
Bally, J., & Langer, W. D. 1982, ApJ, 255, 143
Baulch, D. L., Cox, R. A., Crutzen, P. J., et al. 1982, JPCRD, 11, 327
Blitz, M. A., Dillon, T. J., Heard, D. E., Pilling, M. J., & Trought, I. D. 2004, PCCP, 6, 2162
Burke, P. G., & Taylor, K. T. 1979, JPhB, 12, 2971
Cacciani, P., Brandi, F., Sprengers, J. P., et al. 2002, CP, 282, 63
Cacciani, P., Brandi, F., Velchev, I., et al. 2001, EPJD, 15, 47
Cacciani, P., & Ubachs, W. 2004, JMoSp, 225, 62
Cantù, A. W., Mazzoni, M., Pettini, M., & Tozzi, G. P. 1981, PhRvA, 23, 1223
Chan, W. F., Cooper, G., Sodhi, R. N. S., & Brion, C. E. 1993, CP, 170, 81
Clayton, R. N. 1993, AREPS, 21, 115
Clayton, R. N. 2002, Natur, 415, 860
Clayton, R. N. 2011, in Proc. 74th Annual Meteoritical Society Meeting (Houston, TX: LPI), 5010, https://www.lpi.usra.edu/meetings/metsoc2011/pdf/5010.pdf
Clayton, R. N., Grossman, L., & Mayeda, T. K. 1973, Sci, 182, 485
Davidson, D. F., & Hanson, R. K. 1990, Int. J. Chem. Kinet., 22, 843, http://onlinelibrary.wiley.com/doi/10.1002/kin.550220805/full
Davidson, J. A., Sadowski, C. M., Schiff, H. I., et al. 1976, JChPh, 64, 57
Eidelsberg, M., & Rostas, F. 1990, A&A, 235, 472
Eidelsberg, M., Benayoun, J. J., Viala, Y., & Rostas, F. 1991, Astron. Astrophys. Suppl. Ser., 90, 231
Eikema, K. S., Hogervorst, E. W., & Ubachs, W. 1994, CP, 181, 217
Gao, H., Song, Y., Chang, Y.-C., et al. 2013a, JPCA, 117, 6185
Gao, H., Song, Y., Jackson, W. M., & Ng, C. Y. 2013b, JChPh, 138, 191102
Gao, H., Song, Y., Yang, L., et al. 2011a, JChPh, 135, 221101
Gao, H., Song, Y., Yang, L., et al. 2012, JChPh, 137, 034305
Gao, H., Yang, L., Pan, Y., et al. 2011b, JChPh, 135, 134319
Han, J., Chen, X., & Weiner, B. R. 2000, CPL, 332, 243
Hasegawa, T. I., Herbst, E., & Leung, C. M. 1992, ApJ, 82, 167
Hashizume, K., Takahata, N., Naraoka, H., & Sano, Y. 2011, NatGe, 4, 165
Heays, A. N., et al. 2011, JChPh, 135, 244301
Helm, H., & Cosby, P. C. 1989, JChPh, 90, 4208
Hsu, Y. T., Wang, J. H., & Liu, K. 1997, JChPh, 107, 2351
Husain, D., Mitra, S. K., & Young, A. N. 1974, J. Chem. Soc., Faraday Trans., 70, 1721
Kramida, A., Ralchenko, Y., Reader, J. & NIST ASD Team 2015, NIST Atomic Spectra Database (Gaithersburg, MD: NIST), http://physics.nist.gov/asd
Krot, A. N., et al. 2010, ApJ, 713, 1159
Lahankar, S. A., Zhang, J. M., McKendrick, K. G., & Minton, T. K. 2013, NatCh, 5, 315
Letzelter, C., Eidelsberg, M., & Rostas, F. 1987, CP, 114, 273
Li, X., et al. 2013, A&A, 555, A14
Lin, S. Y., & Guo, H. 2008, JChPh, 129, 124311
Lodders, K. 2003, ApJ, 591, 1220
Lyons, J. 2014, M&PS, 49, 373
Lyons, J., & Young, E. 2005, Natur, 435, 317
Marty, B., Chaussidon, M., Wiens, R. C., Jurewicz, A. J., & Burnett, D. S. 2011, Sci, 332, 1533
McKeegan, K. D., Kallio, A. P., Heber, V. S., et al. 2011, Sci, 332, 1528
McKeegan, K. D., & Leshin, L. A. 2001, RvMG, 43, 279
Moore, C. E. 1993, in Tables of Spectra of Hydrogen, Carbon, Nitrogen, and Oxygen Atoms and Ions, ed. J. W. Gallagher (Boca Raton, FL: CRC Press)
Nakata, P. S., Watanabe, K., & Matsunaga, F. M. 1965, Sci. Light., 14, 54, http://satellite.mpic.de/spectral_atlas/cross_sections/Carbon-oxides/CO2_Nakata(1965)_298K_58.27-114.93nm.txt
Navon, O., & Wasserburg, G. J. 1985, E&PSL, 73, 1

Okabe, H. 1978, Photochemistry of Small Molecules (New York: Wiley)
Okazaki, A., Ebata, T., & Mikami, N. 2001, JChPh, 114, 7886
Okazaki, A., Ebata, T., Sutani, T., & Mikami, N. 1998, JChPh, 108, 1765
Pan, Y., Gao, H., Yang, L., et al. 2011, JChPh, 135, 071101
Pascual, R. Z., Schatz, G. C., Lendvay, G., & Troya, D. 2002, JPCA, 106, 4125
Qi, C., Kessler, J. E., Koerner, D. W., Sargent, A. I., & Blake, G. A. 2003, ApJ,
    597, 986
Qi, C. H., Öberg, K. I., Wilner, D. J., et al. 2013, Sci, 341, 630
Rodgers, S. D., & Charnley, S. B. 2008, MNRAS, 385, L48
Sakamoto, N., Seto, Y., Itoh, S., et al. 2007, Sci, 317, 231
Sheffer, Y., Lambert, D. L., & Federman, S. R. 2002, ApJL, 574, L171
Shi, X. 2012, PhD dissertation, Univ. California
Shi, X., Yin, Q.-Z., Wiens, R., & Ng, C. Y. 2012, LPI, 43, 1403
Song, Y., Gao, H., Chang, Y. C., et al. 2016, ApJ, 819, 23
Stark, G., Huber, K. P., Yoshino, K., Smith, P. L., & Ito, K. 2005, JChPh, 123,
    214303
Stark, G., et al. 2008, JChPh, 128, 114302
Suzuki, T., Shihira, Y., Sato, T., Umemoto, H., & Tsunashima, S. 1993,
    J. Chem. Soc., Faraday Trans., 89, 995
Tang, X., Hou, Y., Ng, C. Y., & Ruscic, B. 2005, JChPh, 123, 074330
Thiemens, M. H., & Heidenreich, J. E. 1983, Sci, 219, 1073

Ubachs, W., Eikema, K. S. E., Levelt, P. F., et al. 1994, ApJL, 427, L55
Ubachs, W., Velchev, I., & Cacciani, P. 2000, JChPh, 113, 547
van Dishoeck, E. F., & Black, J. H. 1988, ApJ, 334, 771
Vieitez, M. O., Ivanov, T. I., Ubachs, W., Lewis, B. R., & de Lange, C. A.
    2008, J. Mol. Liq., 141, 110
Visser, R., van Dishoeck, E. F., & Black, J. H. 2009, A&A, 503, 323
Walter, C. W., Cosby, P. C., & Helm, H. 1993, JChPh, 99, 3553
Walter, C. W., Cosby, P. C., & Helm, H. 2000, JChPh, 112, 4621
Warin, S., Benayoun, J. J., & Viala, Y. P. 1996, A&A, 308, 535
Wiens, R. C., Huss, G. R., & Burnett, D. S. 1999, M&PS, 34, 99
Willacy, K. 2007, ApJ, 660, 441
Willacy, K., Klahr, H. H., Millar, T. J., & Henning, T. 1998, A&A, 338, 995
Willacy, K., & Woods, P. M. 2009, ApJ, 703, 479
Yin, Q.-Z. 2004, Sci, 305, 1729
Yin, Q.-Z., Shi, X. Y., Chao Chang, & Ng, C-Y. 2009, Sci, 324, 1516
Young, E. D. 2007, Sci, 317, 211
Yurimoto, H., & Kuramoto, K. 2004, Sci, 305, 1763
Zhai, H. S., & Han, K. L. 2011, JChPh, 135, 104314
Zhou, J., Lau, K. C., Hassanein, E., et al. 2006, JChPh, 124, 034309
Zhou, S., Xie, D., Lin, S. Y., & Guo, H. 2008, JChPh, 128, 224316
Zipf, E. C., & McLaughlin, R. W. 1978, P&SS, 26, 449